INSTITUTE OF PHYSICS PUBLISHING JOURNAL OF PHYSICS D: APPLIED PHYSICS

J. Phys. D: Appl. Phys. **34** (2001) 1789–1798 www.iop.org/Journals/jd PII: S0022-3727(01)21017-1

Spatial density profiles of the N_2 metastable state $A\,^3\Sigma_u^+$, the $B\,^3\Pi_g$ and $C\,^3\Pi_u$ states in an asymmetric rf discharge

B Krames[1], T Glenewinkel-Meyer[2,3] and J Meichsner[1]

[1] Institut für Physik, Ernst-Moritz-Arndt-Universität, 17487 Greifswald, Germany
[2] Institut für Physik, Technische Universität Chemnitz, 09107 Chemnitz, Germany

E-mail: physik@krames.de and meichsner@physik.uni-greifswald.de

Received 17 January 2001, in final form 18 May 2001

Abstract

A laser-induced fluorescence technique, in combination with optical emission spectroscopy, was applied to investigate the spatial distribution of the number densities of neutral species in an asymmetric low-pressure 27.12 MHz discharge in pure nitrogen. The primary targets of this investigation were the three nitrogen triplet states $C\,^3\Pi_u$, $B\,^3\Pi_g$ and the metastable $A\,^3\Sigma_u^+$ each in their lowest vibrational levels $v = 0, 1, 2$ and additionally $v = 8$ of $A\,^3\Sigma_u^+$ which can be populated very efficiently in the plasma sheath. The absolute number densities of all these states were determined in a Rayleigh scattering experiment, the results of which have been published elsewhere (Krames B, Glenewinkel-Meyer T and Meichsner J 2001 *J. Appl. Phys.* **89** 3115). The spatial profiles as a function of the discharge parameters were studied by varying the gas pressure between 10 and 100 Pa and the effective rf voltage up to 260 V. These profiles of the different molecular states vary markedly in the plasma bulk as well as in the sheath near the powered electrode. A model, which includes the production, diffusion and quenching rates of contributing species and also fluorescence cascade processes, explains these varieties. A comparison with the experimental data at 50 Pa confirms the results of the model calculations.

1. Introduction

The reaction system of interest is an already rather complicated state–state regime of a radio frequency (rf) nitrogen discharge where a whole plethora of reaction partners (electrons, ions, energetic neutrals, radicals, UV and VUV photons) influence particle density distributions as a function of process parameters. Particularly, the electron dynamics in front of the powered discharge electrode is affected by the strong sheath potential modulation in an asymmetric and capacitively coupled rf discharge [1].

An important step towards a complete understanding of the reaction mechanisms at hand is a comparison of experimentally and theoretically determined number densities for all species. Especially, the investigation of the nitrogen molecule triplet states, above all the metastable $A\,^3\Sigma_u^+$, occupies several groups of researchers [2–6]. It is not easy to fully characterize, for example, the population density of an excited molecular state, since all its reactive interactions with other species have to be taken into account [7,8]. Neutral metastables play an important role as carriers of internal energy in excess of several electron volts since they are able to reach the electrode surface by penetrating the plasma sheath.

We will present axial profiles of the absolute number density on the nitrogen metastable triplet state $A\,^3\Sigma_u^+$ and the triplet states $B\,^3\Pi_g$ and $C\,^3\Pi_u$, since their spatial distributions have not yet been published. Our investigations have been limited to the axial component of the spatial distribution. As we shall see, there are unexpected different axial profiles of the excited molecules. For a better understanding of these variations, a model is presented, which rests only on simple assumptions. This has the ability to describe the axial component of the profiles quantitatively, by taking into account diffusion, quenching and cascade as well as excitation processes in the rf plasma sheath.

[3] Present address: Robert-Bosch-GmbH, Department K5/ESM3, Steiermärker Straße 3-5, 70442 Stuttgart, Germany.

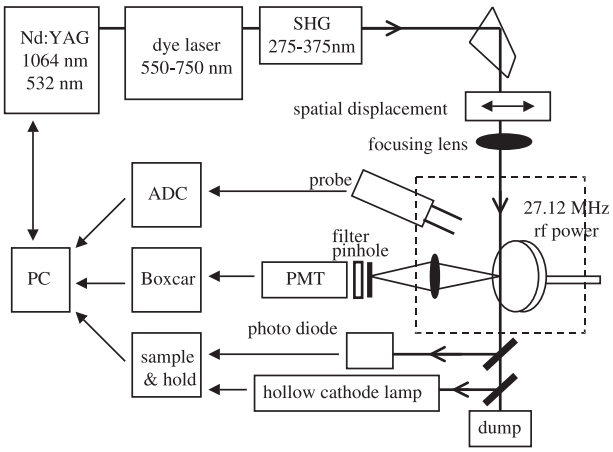

Figure 1. A schematic view of the LIF apparatus, showing the laser system, the vacuum chamber with the driven rf electrode and the electronic equipment. The laser beam enters perpendicular to the axis of optical detection. Both are parallel to the surface of the electrode.

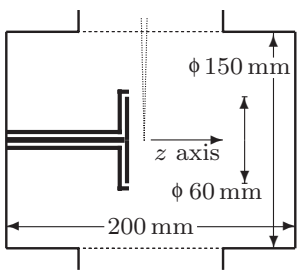

Figure 2. The chamber dimensions viewed in the direction of the laser beam.

The paper is organized as follows. After describing the set-up of the apparatus, we will present our experimental results, the axial number density profiles of the three molecular triplet states and briefly discuss their differences. In addition, dependences on gas pressure and rf voltage will be pointed out. The essential points of the theoretical modelling of the axial profiles will be adumbrated and compared with measured data. We will conclude with a short summary.

2. Experimental details

The apparatus used for the experiments was developed specifically for the *in situ* characterization of the axial relative density profiles of triplet state nitrogen molecules in an rf discharge plasma (figures 1 and 2). An asymmetric discharge between a driven electrode (60 mm diameter) and the grounded walls of the vacuum chamber is generated by a capacitively coupled 27.12 MHz rf power supply. A sustainable plasma ensues between 5 to 100 Pa of nitrogen gas pressure and effective voltage delivered up to 260 V. A pulsed laser beam (8 ns pulse width, 0.1 cm^{-1} spectral width, 1 mJ at 685 nm, 0.3 mJ at 337 nm, 30 Hz repetition rate) excites the plasma species of interest. A photomultiplier (PMT) combined with a boxcar averager detects the time-resolved laser-induced fluorescence (LIF). Spectral filtering (edge and bandpass) as well as spatial filtering reduce scattered laser light and continuous emission from the plasma background. Spatial

Table 1. Absolute number densities of different vibrational states of triplet nitrogen molecules. The data are given for the maximum of the z-dependent distribution function and are valid for a nitrogen pressure of 50 Pa and an effective discharge voltage of 100 V. The missing values were not determined, the error is estimated to be less than 20%. The table is taken from [10].

Vibrational state v	Number density n in cm^{-3}		
	$A\,^3\Sigma_u^+$	$B\,^3\Pi_g$	$C\,^3\Pi_u$
0	9.2×10^{11}	4.8×10^9	1.5×10^6
1	1.3×10^{11}	3.1×10^9	8.7×10^5
2	5.3×10^{10}	1.7×10^9	3.0×10^5
3	—	6.0×10^8	—
4	—	4.5×10^8	—
5	—	3.0×10^8	—
6	—	2.5×10^8	—
7	—	1.3×10^8	—
8	2.7×10^8	7.2×10^7	—
9	—	6.5×10^7	—
10	—	8.5×10^7	—
11	—	6.7×10^7	—
12	—	4.1×10^7	—

filtering is achieved as follows. The laser beam enters the chamber perpendicular to the axis of rotational symmetry of the vessel and the driven electrode (z-axis). It passes parallel to the surface of the electrode and defines the second (x) axis. Perpendicular to both axes mentioned before, the optical detection system (fused silica window, lens, pinhole, optical filter and PMT) defines the third remaining (y) axis. By use of the pinhole in the detection system, we define an active detection volume by the cross section of the laser excitation beam and light detection cone along their respective axes to be about $2 \times 2 \times 1$ mm. This detection volume can be translated along the apparatus z-axis for determination of z-dependent relative density profiles of plasma species. By focusing the laser beam the spatial resolution can be varied down to 300 μm. Triplet states which are not amenable to LIF detection were quantified via optical emission spectroscopy (OES). Here the PMT is replaced by an optical fibre bundle which carries the emitted spontaneous fluorescence light to the entrance slit of a grating monochromator. A cooled charge-coupled device (CCD) camera serves as the detector. In this case, the detection volume is not as well localized as in the LIF experiment and the acceptance cone of this system precludes a direct signal comparison. Therefore, the acceptance cone of the OES was minimized using a second pinhole (5 mm diameter) straight in front of the detection lens thereby improving the spatial resolution. However, several transitions have been measured using both methods and serve as a calibration for those bands that cannot be seen by LIF.

The LIF and OES experiments provide only relative values of the species number densities by spectral integration of the band heads and the whole rotational and fine structures, respectively. Calibration of LIF intensities to absolute densities has been realized by comparison with the signal of a Rayleigh scattering experiment (RS) in pure nitrogen gas, a method which is partly based on a suggestion made by Bogen [9]. The molecular states of interest detected in this experiment comprise the metastable molecular nitrogen triplet state $A\,^3\Sigma_u^+$ and the triplet states $B\,^3\Pi_g$ and $C\,^3\Pi_u$. The $A\,^3\Sigma_u^+$

Table 2. Implementations of the experiments done by LIF and OES.

Excitation	Fluorescence	Method
$A\,^3\Sigma_u^+, v=0$	$\rightarrow B\,^3\Pi_g, v=5 \rightarrow A\,^3\Sigma_u^+, v=3$	LIF
$A\,^3\Sigma_u^+, v=0$	$\rightarrow B\,^3\Pi_g, v=3 \rightarrow A\,^3\Sigma_u^+, v=1$	LIF
$A\,^3\Sigma_u^+, v=1$	$\rightarrow B\,^3\Pi_g, v=6 \rightarrow A\,^3\Sigma_u^+, v=3$	LIF
$A\,^3\Sigma_u^+, v=2$	$\rightarrow B\,^3\Pi_g, v=7 \rightarrow A\,^3\Sigma_u^+, v=4$	LIF
$A\,^3\Sigma_u^+, v=8$	$\rightarrow B\,^3\Pi_g, v=12 \rightarrow A\,^3\Sigma_u^+, v=9$	LIF
$B\,^3\Pi_g, v=0$	$\rightarrow C\,^3\Pi_u, v=0 \rightarrow B\,^3\Pi_g, v=1$	LIF
$B\,^3\Pi_g, v=0$	$\rightarrow C\,^3\Pi_u, v=1 \rightarrow B\,^3\Pi_g, v\geqslant 1$	LIF
$B\,^3\Pi_g, v=1$	$\rightarrow C\,^3\Pi_u, v=2 \rightarrow B\,^3\Pi_g, v\geqslant 2$	LIF
	$B\,^3\Pi_g, v=1 \rightarrow A\,^3\Sigma_u^+, v=0$	OES
	$B\,^3\Pi_g, v=2 \rightarrow A\,^3\Sigma_u^+, v=0$	OES
	$C\,^3\Pi_u, v=0 \rightarrow B\,^3\Pi_g, v=0$	OES
	$C\,^3\Pi_u, v=1 \rightarrow B\,^3\Pi_g, v=0$	OES
	$C\,^3\Pi_u, v=2 \rightarrow B\,^3\Pi_g, v=1$	OES

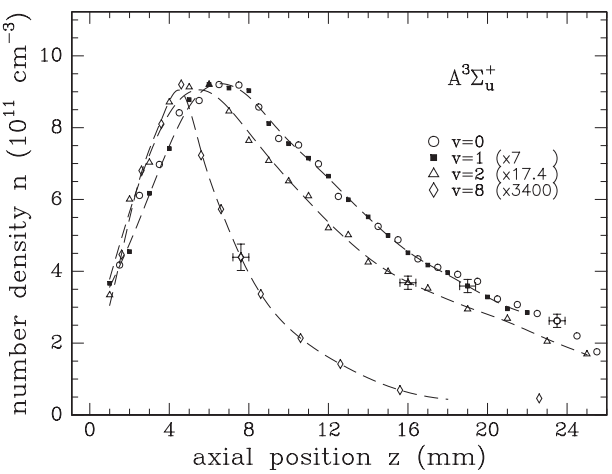

Figure 3. Axial number density profile of $A\,^3\Sigma_u^+$, $v=0$. The densities of $v=1, 2$ and 8 are multiplied by 7, 17.4 and 3400, respectively, to standardize the profiles to each maximum, measured by LIF at $p=50$ Pa and $U_{\text{eff}}=100$ V.

and $B\,^3\Pi_g$ states have been measured and calibrated by LIF and RS respectively. Due to missing convenient intermediates for LIF detection of the $C\,^3\Pi_u$ state and its short radiative lifetime, absolute calibration was performed solely by OES comparing simultaneous LIF and OES results on the $B\,^3\Pi_g$ state with the OES signal intensities for the $C\,^3\Pi_u$ state. Optical saturation due to the high laser light intensities is not negligible, but is taken into account by the calculations of the calibration. The results for the calibrated number densities differ by about seven orders of magnitude from as much as 10^{12} cm^{-3} down to almost 10^5 cm^{-3} and are given in table 1. The calibration has been published in detail previously [10].

The detailed band designations of all experiments to determine density profiles are composed in table 2. Laser-induced fluorescence spectroscopy was used to determine the number density of the metastable triplet states $A\,^3\Sigma_u^+$ with the vibrational quantum numbers $v=0, 1, 2$ and 8 as well as the triplet state $B\,^3\Pi_g$ with vibrational numbers $v=0$ and 1. The measurement of $A\,^3\Sigma_u^+$, $v=0$, for example, was done by laser excitation into the $B\,^3\Pi_g$, $v=5$ and detection of the fluorescence of the radiative decay into $A\,^3\Sigma_u^+$, $v=3$. The determination of the axial density profiles of the triplet states $B\,^3\Pi_g$, $v=2$ and $C\,^3\Pi_u$ with $v=0, 1$ and 2 was done by optical emission spectroscopy.

The plasma density and the electron temperature can be estimated using a passively compensated Langmuir probe and a double probe which can be moved axially inside the vessel. While the diameter of the platinum wire probe tip was 200 μm, the spatial resolution of the probe was about 0.5 mm.

3. Results and discussion

Firstly we describe several measured density profiles for a fixed set of discharge parameters. The gas pressure p was chosen to be 50 Pa and the effective discharge voltage U_{eff} to be 100 V. Further on, the dependence of the profiles on pressure variation is shown. The last subsection deals with the dependence on different values of rf power.

3.1. Spatial profiles at 50 Pa

The axial density profiles of $A\,^3\Sigma_u^+$, $v=0, 1, 2, 8$ recorded by LIF are shown in figure 3. The abscissa defines the axial position, i.e. the distance from the powered electrode. The number densities of the species indicated on the ordinate are standardized to the maximum of $A\,^3\Sigma_u^+$, $v=0$ to point out the differences in shape between various profiles. However, normalization factors are given for comparison on the absolute scale. The error bars are given for some points signifying the reproducibility of all the data. The specific vibrational levels of $A\,^3\Sigma_u^+$ show different axial density profiles. The two lowest levels $v=0$ and 1 have a broad distribution with its maximum at approximately 6.5 mm from the electrode. For higher vibrational quantum numbers the profile narrows and the maximum moves toward the electrode. The most narrow axial distribution measured belongs to $v=8$ and has its peak value at $z=4.3$ mm. The density shows a much stronger decrease at longer distances from the electrode than for other vibrational states of $A\,^3\Sigma_u^+$.

Figures 4 and 5 display the density of the triplet states $B\,^3\Pi_g$ and $C\,^3\Pi_u$ with vibrational quantum numbers $v=0$, 1 and 2. In those graphs the respective three standardized profiles seem to be identical in their spatial behaviour. But the maximum density is reached at $z=3.9$ mm for the $B\,^3\Pi_g$ state and $z=3.5$ mm for the $C\,^3\Pi_u$ state. While the $C\,^3\Pi_u$ densities were measured solely by OES, the different levels of $B\,^3\Pi_g$ were determined both by OES and LIF. The agreement between the LIF and OES results is fairly good and ratifies the correct choice of spatial resolution for the optical system used by OES. Note that the measured intensities of the $C\,^3\Pi_u$ are temporally averaged, since its radiation lifetime is comparable with the period of the radio frequency ($\approx$37 ns).

In order to classify the different profiles and peak positions we have to look at the axial distribution of the plasma density. Figure 6 shows the axial variation of the plasma ion number density and the electron temperature, assuming singly charged molecular nitrogen ions and the electron energy distribution to be Maxwellian. The plasma density n_i was determined by calculating the electron temperature T_e at the floating potential of the electrical double probe and by analysing the ion saturation current using the methods according to Johnson, Malter and Sonin, respectively. Additionally the electron temperature was determined by analysing the gradient in a semi-logarithmic plot of the Langmuir probe characteristics in

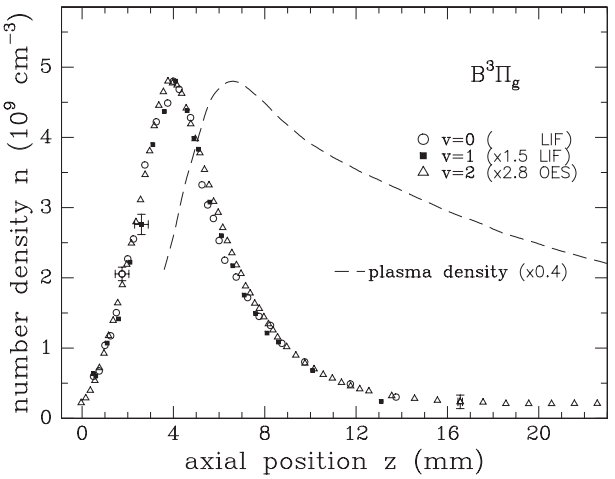

Figure 4. Axial number density profile of B $^3\Pi_g$, $v = 0$. The densities of $v = 1$ and 2 are multiplied by 1.5 and 2.8 respectively, to standardize the profiles to each maximum, measured by LIF and OES at $p = 50$ Pa and $U_{\text{eff}} = 100$ V.

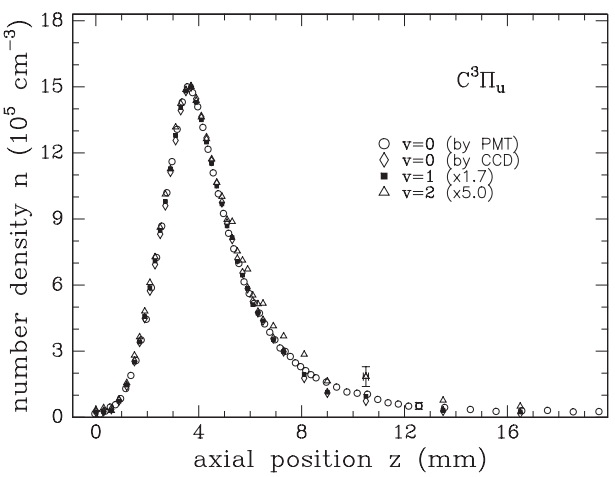

Figure 5. Axial number density profile of C $^3\Pi_u$, $v = 0$. The densities of $v = 1$ and 2 are multiplied by 1.7 and 5, respectively, to standardize the profiles to each maximum, measured by OES with the CCD and PMT at $p = 50$ Pa and $U_{\text{eff}} = 100$ V.

the region of the electron current close to the floating potential. To demonstrate the axial profile of the ion number density qualitatively, the ion saturation current I_{IS} measured by the Langmuir probe is also shown in figure 6. The result for T_e of both methods is about 1 eV in the plasma bulk and varies only in the range of the estimated errors.

From the strong decrease of the measured ion density and the sharp increase of the electron temperature towards the powered electrode ($z = 0$ mm) we can identify the thickness of the plasma sheath. In our experiments at 50 Pa we estimate the maximum sheath thickness to be about $z_0 = 5.3$ mm. The comparison of this result with the profiles in figures 3–5 shows that the short-lived states C $^3\Pi_u$, B $^3\Pi_g$ and A $^3\Sigma_u^+$, $v = 8$ have their maximum number densities inside the sheath region and not in the region of maximum plasma density. We therefore infer that they are not produced predominantly in the plasma bulk but by direct electron impact in the pulsating rf sheath. In contrast, the long-lived species A $^3\Sigma_u^+$, $v = 0, 1$ exhibit axial density profiles similar to the plasma density distribution;

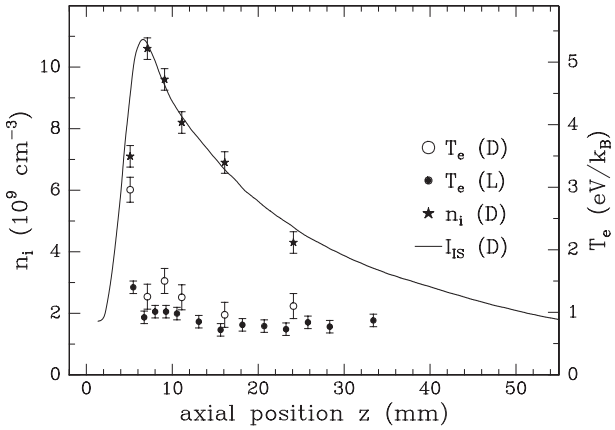

Figure 6. Axial plasma density profile $n_i(z)$ measured with an electrical double probe (D) and electron temperature T_e measured by Langmuir (L) and double (D) probes. Additionally, the axial profile of the ion saturation current I_{IS} is shown, standardized to n_i, at $p = 50$ Pa and $U_{\text{eff}} = 100$ V.

even the maxima seem to be at the same distance from the electrode. This similarity does not necessarily imply that the lower vibrational levels of A $^3\Sigma_u^+$ are produced by the plasma bulk electrons. We will discuss a different mechanism in section 4 by a simple model of the axial profiles.

3.2. Pressure dependence

The pressure dependence of the axial profiles has been studied from 10 to 100 Pa. The distributions of all investigated states show the expected behaviour: increasing the gas pressure p the maxima of the density move towards the powered electrode and the slope of the profiles becomes steeper.

With regard to earlier investigations [11, 12] the pressure dependence of the spatial plasma density distribution measured by probe experiments can be described with the aid of an empirical similarity parameter z^2p. Plotted against this parameter the standardized plasma density profiles merge into one standardized axial profile.

The axial density profiles of all investigated N_2 states have been tested, if there is any similarity parameter as for the plasma density. The short-lived triplet states C $^3\Pi_u$, B $^3\Pi_g$ and A $^3\Sigma_u^+$, $v = 8$ do not indicate any convincing similarity behaviour. In contrast, the pressure dependence of the long-lived states A $^3\Sigma_u^+$, $v = 0, 1$ shows an excellent conformity in terms of the same similarity parameter as for the plasma density (ditto z^2p) for both vibrational states. Figure 7 displays an example of the results for A $^3\Sigma_u^+$, $v = 0$, measured at gas pressures of 30, 50 and 100 Pa at $U_{\text{eff}} = 100$ V. The standardized intensities are plotted versus the similarity parameter z^2p. The agreement over three orders of magnitude from 10^2–10^5 mm^2 Pa is clearly visible. Due to the long radiative and collisional lifetime, the spatial density variation of the A $^3\Sigma_u^+$, $v = 0, 1$ is dominated by diffusion, which scales with $D\partial^2/\partial z^2$. Considering the diffusion coefficient D to be inversely proportional to pressure p, we arrive at the factor z^2p as an obvious similarity parameter.

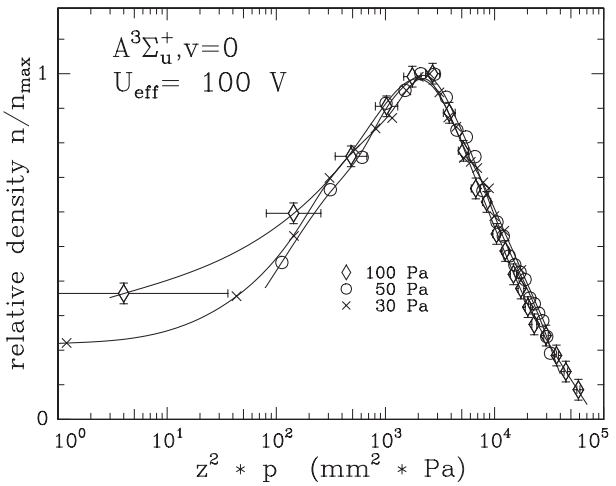

Figure 7. Axial number density profile of $A\,^3\Sigma_u^+$, $v = 0$ standardized plotted versus the similarity parameter $z^2 p$, measured at the gas pressures of 30, 50 and 100 Pa and $U_{\text{eff}} = 100$ V.

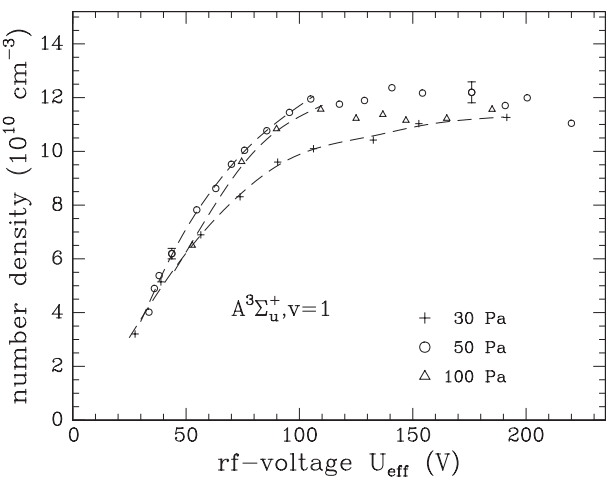

Figure 8. Number density of $A\,^3\Sigma_u^+$, $v = 1$ at a distance $z = 6.5$ mm from the electrode plotted versus the rf voltage for three different pressures. The error bars are shown exemplarily.

3.3. The rf power dependence

The effective rf voltage U_{eff} is used as a parameter for the power transferred into the plasma. In general, this voltage is not directly proportional to the rf power, but the experimental results of this work have shown that, in fact, it is a suitable parameter to characterize the energy input.

The rf power dependence is given using the values of absolute number densities at the peak of the spatial profiles, which have been calibrated using an additional Rayleigh scattering experiment [10]. Our investigations have been limited to a gas pressure of 50 Pa.

The shape of the density profiles of the long-lived states $A\,^3\Sigma_u^+$, $v = 0$, 1 do not vary with increasing rf power. This can also be stated for gas pressures of 30 and 100 Pa. However, with increasing rf voltage the number density of $A\,^3\Sigma_u^+$, $v = 1$ rises for all pressures, see figure 8. At a voltage of about $U_{\text{eff}} = 100$ V a maximum is reached and the density remains constant. The same behaviour can be found for the vibrational ground state of $A\,^3\Sigma_u^+$. Its density as a function of rf voltage

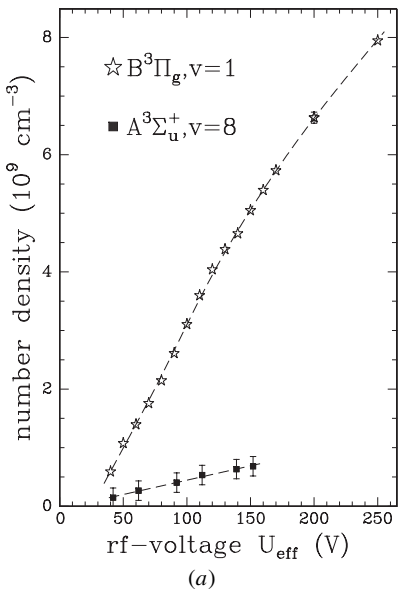

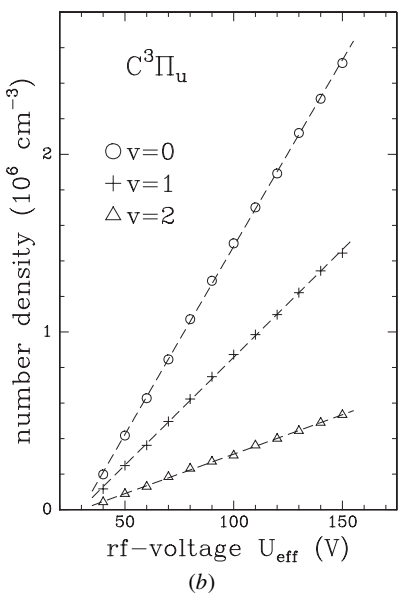

Figure 9. Maximum number density of the lower vibrational states of $C\,^3\Pi_u$ and $B\,^3\Pi_g$ and the higher vibrational excited state $A\,^3\Sigma_u^+$, $v = 8$ plotted versus the rf voltage at $p = 50$ Pa. The error bars are shown exemplarily.

also shows a saturation effect which can be explained by a significant self-quenching rate and increasing density of nitrogen atoms, which have not been detected in this work. The possible self-quenching of the two lowest vibrational states of $A\,^3\Sigma_u^+$ will be taken into account in the context of the model in section 4.

The short-lived triplet states $C\,^3\Pi_u$, $B\,^3\Pi_g$ and $A\,^3\Sigma_u^+$, $v = 8$ show an rf power dependence which is different from that discussed above. Here, the $A\,^3\Sigma_u^+$, $v = 8$ state is also called short-lived due to its very effective deactivation by quenching. In figure 9 the number densities are plotted versus the rf voltage U_{eff} at a pressure of 50 Pa each at the point of maximum density, $z = 5$ mm for $A\,^3\Sigma_u^+$, $v = 8$ and $B\,^3\Pi_g$, $v = 1$ and $z = 4$ mm for $C\,^3\Pi_u$, $v = 0, 1, 2$. The densities of the all short-lived states increase linearly with rf voltage. No saturation effect is observed at the voltages used.

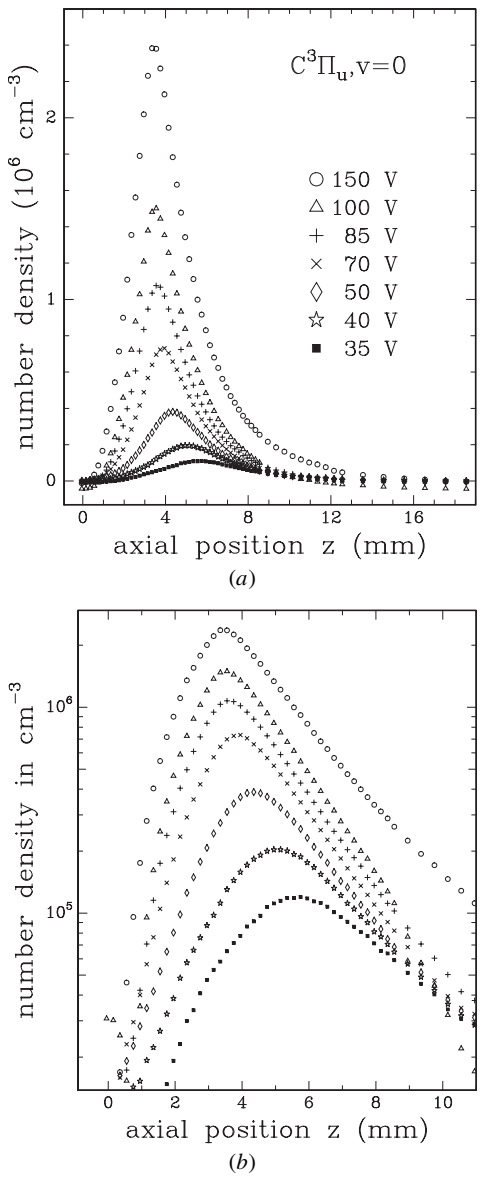

Figure 10. Axial number density profiles of $C\,^3\Pi_u$, $v = 0$ for seven different rf voltages U_{eff} at $p = 50$ Pa: (*a*) linear and (*b*) half-logarithmic with expanded x-axis. The error bars are smaller than the plotted symbols.

In contrast to the lower vibrational levels of $A\,^3\Sigma_u^+$, $v = 0, 1$ the short-lived triplet states $C\,^3\Pi_u$ and $B\,^3\Pi_g$ do exhibit a change in shape of the axial density profiles when the rf power varies. Figure 10 provides an example for these triplet states showing, for $C\,^3\Pi_u$, $v = 0$, the axial number density distribution at seven different rf voltages between 35 and 150 V. At very low rf voltages the maximum of the axial profiles shifts to greater distances from the electrode. To display this effect more clearly the same curves are plotted in figure 10(*b*) on a semi-logarithmic scale with an expanded x-axis. From 150 down to 85 V the distance of the density maximum from the powered electrode remains constant at about $z = 3.5$ mm. However, from 70 down to 35 V the spacing increases up to 5.8 mm. For $B\,^3\Pi_g$ this displacement of the maximum density occurs at comparable distances from about 3.8–6.0 mm. At still lower values of the rf voltage the discharge extinguishes.

4. Modelling of the axial profiles

The model is divided into two parts. Firstly, we investigate the main production process for the triplet states, which we suspect to be excitation directly from the ground state by electron impact in the plasma sheath region. We compute spatially resolved production rates which serve as input to the model of stationary axial number density profiles depending on production, diffusion and several deactivation processes of the different triplet states in the second step.

Due to the difference in length scales between the diameter of the powered electrode and the much smaller extent of the investigated discharge zones we can assume a uni-dimensional problem. Therefore the model deals with only one spatial coordinate z which identifies the distance from the powered electrode ($z = 0$ mm) along the symmetry axis of the whole vessel.

4.1. Excitation by electron impact in the sheath

The starting point is the continuity equation for the electric current from the powered electrode. This ac current with rf frequency results in an electron current density which drives the pulsating plasma sheath edge. The spatial distribution of the ion density in the sheath region is taken as being static and varies with distance z as follows, (from [1]):

$$n_i(z) = n_0(1 - z/z_0)^{-1/2} \qquad \text{with} \qquad 0 \leqslant z < z_0. \quad (1)$$

Here, n_0 is the ion number density right in front of the electrode and z_0 is the maximum thickness of the plasma sheath. If the driving rf current is sinusoidal in time, we get the following formula for the uni-dimensional space-time curve $z_k(t)$ of the sheath edge:

$$z_k(t) = z_0\left(1 - \cos^4\left(\tfrac{1}{2}\omega t\right)\right) \qquad \text{with} \quad z_0 = \frac{I_0}{n_0 e \omega A_e}. \quad (2)$$

Here, z_0 is given by I_0, the amplitude of the driving rf current, with frequency ω and the area of the electrode surface A_e. Using this formula we can compute the velocity $\dot{z}_k(t)$ of the sheath edge. By reinserting $z_k(t)$ into the equation of $\dot{z}_k(t)$ we can eliminate the explicit time dependence

$$\dot{z}_k(t) = 2\omega z_0 \sin\left(\tfrac{1}{2}\omega t\right)\cos^3\left(\tfrac{1}{2}\omega t\right)$$
$$|\dot{z}_k|\Big|_{z=z_k} = 2\omega z_0\sqrt{\left(1 - \frac{z_k}{z_0}\right)^{3/2} - \left(1 - \frac{z_k}{z_0}\right)^2} \quad (3)$$

and we obtain the velocity of the edge at the distance $z = z_k$ from the electrode. This is also the mean velocity of an electron in the edge. Electrons, which undergo collisions with the gas molecules while the sheath is expanding, relapse into the space-charge region and are accelerated by the electric field to even higher velocities than they had before the collision. Assuming this elastic scattering to be isotropic we can presume the mean electron velocity after collision and acceleration to be twice the previous velocity [13]. On condition that all electrons eventually undergo collisions we can derive the space-time distribution of the mean electron energy kT_k in the oscillating sheath region, simplified, assuming their velocity distribution to be Maxwellian with $kT_k = \frac{1}{2}m_e(2\dot{z}_k)^2$.

Now we have to add the collisional excitation cross sections of the investigated molecular states to our model. The data on electron impact cross sections and their energy dependence were taken from several references [14–17]. Furthermore, we have to define an effective penetration depth λ_{eff} of the highly energetic electrons into the plasma bulk which is assumed to be larger than the mean free path because of their much higher velocity and strongly directional movement.

Integration over one cycle of the rf ($\nu = 27.12$ MHz) oscillation, which can be expressed as an integration over z_k from 0 to z, results in the axial excitation rate $R(z)$, which is specific for each vibrational triplet state with energy level W_0 above the vibrational ground state. Note that the 'sheath edge electron temperature' T_k also depends on the integration variable z_k:

$$R(z) = 3.25 n_G n_0 \sigma_0 \frac{\omega}{2\pi} \int_0^z \left(1 + \frac{3}{2}\frac{kT_k}{W_0}\right)^{-3/2} \left(1 - \frac{z_k}{z_0}\right)^{-1/2} \times \exp\left(-\frac{W_0}{kT_k} - \frac{z - z_k}{\lambda_{\mathrm{eff}}}\right) \mathrm{d}z_k \quad (4)$$

$$\text{with} \quad kT_k = 8 m_e z_0^2 \omega^2 \left(\left(1 - \frac{z_k}{z_0}\right)^{3/2} - \left(1 - \frac{z_k}{z_0}\right)^2\right).$$

Here, n_G is the gas number density and σ_0 is the maximum of the energy-dependent cross section. The maximum sheath thickness z_0 can be taken from the results of the probe measurements. At a gas pressure of 50 Pa and an rf voltage of $U_{\mathrm{eff}} = 100$ V it amounts to $z_0 \approx 5.3$ mm.

The integral must be solved numerically. The two parameters λ_{eff} and n_0 are unknown and can be obtained by a fit to the measured density profile of the $C\,^3\Pi_u$, $v = 0$ or $v = 1, 2$ states. Due to their short radiative lifetime of about $\tau = 38$ ns we can disregard the effects of diffusion and deactivation by quenching. The density profile is then only determined by excitation $R(z)$ and radiative decay and we can write,

$$0 = R_C(z) - A_{ij} n_C(z) \quad (5)$$

where A_{ij} is the Einstein coefficient and n_C is the number density of a single vibrational level of $C\,^3\Pi_u$. From the measured axial profiles of the three vibrational levels at $p = 50$ Pa and $U_{\mathrm{eff}} = 100$ V a fit yielded averaged values $n_0 = (3.6 \pm 0.7) \times 10^8$ cm^{-3} and $\lambda_{\mathrm{eff}} = (1.67 \pm 0.05)$ mm.

The ion concentration n_0 right in front of the electrode turns out to be two orders of magnitude lower than the ion density in the bulk plasma ($n_{i,\max} \approx 1.2 \times 10^{10}$ cm^{-3}). This effect was expected and agrees with other published data [18–21].

The resulting effective penetration depth λ_{eff} for the directional movement of the higher energy electrons ($W_e \geqslant W_0$) turns out to be two times greater than the mean free path of the lower energy plasma electrons with $\lambda_e \approx 0.75$ mm.

Figure 11 exemplifies the production rate in absolute values for the states $A\,^3\Sigma_u^+$, $v = 0, 8$, $B\,^3\Pi_g$, $v = 0$ and $C\,^3\Pi_u$, $v = 0$ calculated from equation (4) on a logarithmic scale at 50 Pa. Although the electron energy necessary for the excitation of $A\,^3\Sigma_u^+$, $v = 0$ is much lower than for $C\,^3\Pi_u$, the production rate of $C\,^3\Pi_u$ is two orders of magnitude higher, due to the much larger excitation cross section.

Except for the absolute values the production rate profiles seem to be very similar. However, the maximum rate of the states with lower excitation energy occurs at a slightly larger distance from the electrode than for the higher energy levels. This is due to the axial variation of the electron kinetic energy in the plasma sheath.

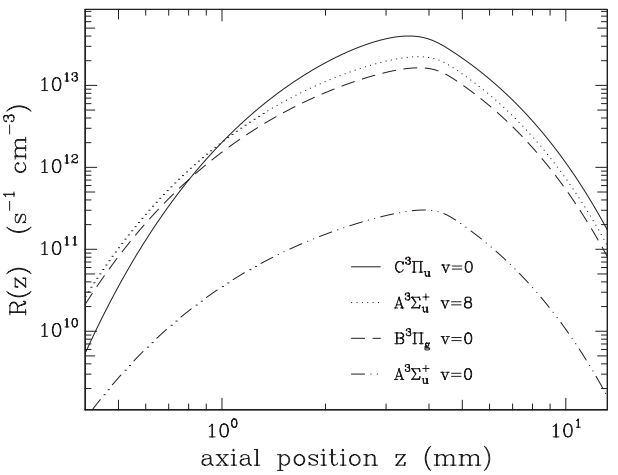

Figure 11. Axial profiles of the production rate $R(z)$ for the states $A\,^3\Sigma_u^+$, $v = 0, 8$, $B\,^3\Pi_g$, $v = 0$ and $C\,^3\Pi_u$, $v = 0$ calculated from equation (4) with $z_0 = 5.3$ mm, $n_0 = 3.6 \times 10^8$ cm^{-3} and $\lambda_{\mathrm{eff}} = 1.67$ mm at $p = 50$ Pa.

4.2. Loss and transport processes

In contrast to the above discussion for the $C\,^3\Pi_u$ state, for the longer-lived species $B\,^3\Pi_g$ and $A\,^3\Sigma_u^+$ we have to take several other processes into account, such as radiation cascade processes, collisional quenching and diffusion. The radiative decay cascade $C\,^3\Pi_u \rightarrow B\,^3\Pi_g \rightarrow A\,^3\Sigma_u^+$ leads to a depletion of the higher excitation levels and to an additional formation of lower excited species. In addition, in the model we have to consider the collisional reactions between the species listed below:

$$N_2(X\,^1\Sigma_g^+) + e \xrightarrow{W_{\mathrm{kin}}} N_2(C\,^3\Pi_u, v') + e \quad (6)$$

$$N_2(X\,^1\Sigma_g^+) + e \xrightarrow{W_{\mathrm{kin}}} N_2(B\,^3\Pi_g, v') + e \quad (7)$$

$$N_2(X\,^1\Sigma_g^+) + e \xrightarrow{W_{\mathrm{kin}}} N_2(A\,^3\Sigma_u^+, v') + e \quad (8)$$

$$N_2(C\,^3\Pi_u, v') \xrightarrow{A_{v'v''}} N_2(B\,^3\Pi_g, v'') + h\nu \quad (9)$$

$$N_2(B\,^3\Pi_g, v') \xrightarrow{A_{v'v''}} N_2(A\,^3\Sigma_u^+, v'') + h\nu \quad (10)$$

$$N_2(A\,^3\Sigma_u^+, v') \xrightarrow{A_{v'v''}} N_2(X\,^1\Sigma_g^+, v'') + h\nu \quad (11)$$

$$N_2(A) + N_2(A) \xrightarrow{k_1} N_2(X) + N_2(B, v') \quad (12)$$

$$N_2(A) + N_2(A) \xrightarrow{k_2} N_2(X) + N_2(C, v') \quad (13)$$

$$N_2(A, v') + N(^4S) \xrightarrow{k_3} N_2(X, v'') + N^* \quad (14)$$

$$N_2(A, v' \geqslant 2) + N_2(X, v'') \xrightarrow{k_4} N_2(A, v' - 2) + N_2(X, v'' + 1) \quad (15)$$

$$N_2(A) + N_2(X, v) \longrightarrow N_2(B) + N_2(X, v') \quad (16)$$

$$N_2(B, v') + N_2 \xrightarrow{k_5} N_2(W,\ A \text{ or } X, v'') + N_2 \quad (17)$$

$$N_2(C, v') + N_2 \xrightarrow{k_6} N_2 + \text{other particles.} \quad (18)$$

The corresponding rate coefficients are listed in table 3. Equations (6)–(8) describe the formation of the triplet states

by direct electron impact. Radiative cascade processes are given by equations (9)–(11). These are important branches for the production of the $B\,^3\Pi_g$ and $A\,^3\Sigma_u^+$ states. Equations (12)–(13) signify the self-quenching processes of $A\,^3\Sigma_u^+$, which represent the formation processes of $B\,^3\Pi_g$ and $C\,^3\Pi_u$ states. Equation (14) describes the quenching of $A\,^3\Sigma_u^+$ by atomic nitrogen. In pure nitrogen discharges the dissociation rate is comparatively high because surface recombination is very slow. For example, Adams and Miller [22] have shown a recombination probability in N_2 pulsed rf discharges of 0.75% at 1 Torr for stainless-steel surfaces. However, in discharges comparable with ours, the proportion of the concentrations of N(^{4}S) atoms and metastable $A\,^3\Sigma_u^+$ state molecules is given by $n(\mathrm{N})/n(\mathrm{N_2(A)}) \approx 10$ by some authors [23]. With this factor and the measured number density of $A\,^3\Sigma_u^+$ we can estimate the atom density to be about 10^{13} cm^{-3}. This is equal to the dissociation ratio of 10^{-3}. Unfortunately this assumption is insufficient to model the quenching by reaction (14) in full, due to its unknown axial distribution. But we can assume the quenching frequency to be approximately as high as that of reaction (12) for the lower vibrational levels. So we have to consider a factor of two for the error of our modelled quenching rates. For the loss of higher vibrational levels of $A\,^3\Sigma_u^+, v \geqslant 2$, reaction (14) is more important but collisions with gas molecules in ground state $X\,^1\Sigma_g^+$ (equation (15)) become dominant with increasing vibration. This is a very effective quenching process, for example, for $A\,^3\Sigma_u^+$, $v = 8$ for which reaction (14) is negligible.

The associative process (16) is another important quenching reaction [24], particularly if the vibrational temperature of $X\,^1\Sigma_g^+$, v is very high, maybe higher than that of $A\,^3\Sigma_u^+$, v. But, at the same time, the reaction is a formation process of $B\,^3\Pi_g$, v' states. At the gas pressure used in our work, about half the total loss rate of $B\,^3\Pi_g$ occurs via radiative decay into the metastable $A\,^3\Sigma_u^+$ state. The collisional quenching of $B\,^3\Pi_g$ forms $X\,^1\Sigma_g^+$, $A\,^3\Sigma_u^+$ or $W\,^3\Delta_u$ states (reaction (17)). Most of the metastable $W\,^3\Delta_u$ state converts back into $B\,^3\Pi_g$ again by collisional quenching. So formation of $A\,^3\Sigma_u^+$ by reaction (17) can be assumed to contribute to more than 90% [23]. Altogether we can assume that most of the $B\,^3\Pi_g$ state molecules convert back into the metastable $A\,^3\Sigma_u^+$ state, by radiative decay but also by collisional quenching processes. So, in our model of a stationary plasma reaction, equation (16) will not affect the number density profiles, but it shifts the distribution of the vibrational population of the $A\,^3\Sigma_u^+$ state. Due to the lack of knowledge of the $X\,^1\Sigma_g^+$ vibrational distribution we are not able to account for this shift. Only for the quenching of the $A\,^3\Sigma_u^+$, $v = 8$ will this cause a non-vanishing underestimation by the model. Reaction (18) describes the collisional quenching of $C\,^3\Pi_u$, which is negligible in comparison to equation (9).

Due to diffusion, the long-lived species are able to reach the walls of the chamber, especially the surface of the electrode. These kinds of collisions are an important loss process for $A\,^3\Sigma_u^+$. This will be included by a boundary condition based on a suggestion made by Fujimoto *et al* [25]:

$$\frac{\partial}{\partial z} n(z) = \frac{1-\alpha}{1+\alpha} \frac{\overline{v}_{\mathrm{th}}}{2D} n(z) \qquad \text{at position} \quad z = 0. \tag{19}$$

Here, $\overline{v}_{\mathrm{th}}$ is the mean thermal velocity and $n(z)$ the number density of the considered species. D is the diffusion coefficient and α is the reflection coefficient. The latter is defined as the probability for an excited molecule to keep its excitation energy after a collision with the wall. Therefore the wall material plays an important role. For quartz, one can find values of α between 60% and 83% [25,26]. The reflection coefficient of walls built of stainless steel, such as used in this work, is assumed to be much lower [27]. Due to the comparison between the results of our model and our experimental data, the reflection coefficient of $A\,^3\Sigma_u^+$, $v = 0$ can only be estimated to <50% [13].

The second boundary condition is

$$\lim_{z \to \infty} n(z) = 0. \tag{20}$$

At very long distances, the density has to vanish. Derived from the equation of continuity the following equation is used for modelling stationary axial number density profiles.

$$D \frac{\partial^2}{\partial z^2} n(z) - k_{\mathrm{S}} n(z)^2 - k_{\mathrm{L}} n(z) + P(z) = 0 \qquad \text{with} \qquad k_{\mathrm{L}} = A_{v',v''} + \sum_i k_i n_i. \tag{21}$$

The first term specifies the diffusion current and in the second the deactivation processes with squared number density dependence are summarized by k_{S}. Linear loss terms can be collected into the coefficient k_{L}. The production term $P(z)$ takes account of formation by electron impact in the sheath region $R(z)$ as well as the above-mentioned production by cascade processes for $B\,^3\Pi_g$ and $A\,^3\Sigma_u^+$. In addition, the formation of lower energy states by processes from equation (15) has been taken into account. We can assume that $C\,^3\Pi_u$ is produced only by direct electron impact, and we can neglect all other formation processes [28, 29]. (Due to its fast decay we calculate the time-averaged number density of $C\,^3\Pi_u$.)

4.3. Comparison with the experimental results

With the aid of our model, the axial number densities of all investigated triplet states can be calculated and compared with the experimental results. In figure 12, the axial number density profiles of the triplet states $A\,^3\Sigma_u^+$, $v = 0, 1, 2, 8$, $B\,^3\Pi_g$, $v = 0, 1, 2$ and $C\,^3\Pi_u$, $v = 0, 1, 2$ are illustrated under our most commonly used discharge parameters, $U_{\mathrm{eff}} = 100$ V and $p = 50$ Pa. For the sake of clarity the particular profiles are normalized and displayed by lines instead of separate symbols for each data point. The measured experimental results are plotted in figure 12(*a*) and can be qualitatively compared to the calculated results from the model (figure 12(*b*)).

The shape of the experimental curves is rendered quite satisfactory by the calculated profiles. A more exact analysis can be carried out with the aid of three characteristic parameters. Table 4 contains the axial position $z_{\max}$ of the maximum number density, the broadening expressed by the full width at half maximum of the profiles and the maximum number density $n_{\max}$ for each species. All positions of the experimental maxima are reproduced very well by the model. However, for the lowest triplet states $A\,^3\Sigma_u^+$, $v = 0, 1$ there is

Table 3. Collisional reaction rate coefficients k_{1-6} used with v' from reactions (12)–(15) and (17)–(18). Values for k_1 and k_2 apply to $A\,^3\Sigma_u^+, v = 0$. Values for $A\,^3\Sigma_u^+$, $v = 1$ are similar.

	Rate coefficient (10^{-11} cm^{3}s^{-1}) with v'					
v'	k_1	k_2	k_3	k_4	k_5	k_6
0	—	2.6	5	0	1	1.4
1	24	4.1	6.5	0	1.2	3.7
2	39	4.1	6.5	0.0005	1.6	8
3	19	2.8	0	0.0038	2.54	8.8
4	16	1.0	5	0.013	2.43	—
5	15	—	5	0.026	2.8	—
6	11	—	5	0.051	3.2	—
7	9	—	5	0.24	5.5	—
Refs	[30,31]	[32–34]	[35,36]	[37,38]	[8,39,40]	[41–44]

Table 4. The position z_{max} of the maximum, the full width at half maximum (FWHM) of the profiles and the maximum number density n_{max} for each species at $p = 50$ Pa and $U_{eff} = 100$ V. The experimental data are compared with the model data.

State	z_{max} (mm)		FWHM (mm)		n_{max} (cm^{-3})	
	Data	Model	Data	Model	Data	Model
$A\,^3\Sigma_u^+, v = 0$	6.5 ± 0.2	6.0	14.0 ± 0.5	16.9	9.2×10^{11}	1.4×10^{11}
$A\,^3\Sigma_u^+, v = 2$	5.4 ± 0.2	5.2	12.1 ± 0.5	13.1	5.3×10^{10}	2.0×10^{10}
$A\,^3\Sigma_u^+, v = 8$	4.3 ± 0.1	4.4	6.0 ± 0.3	7.2	2.7×10^{8}	4.4×10^{8}
$B\,^3\Pi_g, v = 0$	3.9 ± 0.1	3.9	4.1 ± 0.2	3.9	4.8×10^{9}	2.2×10^{9}
$C\,^3\Pi_u, v = 0$	3.5 ± 0.1	3.5	3.0 ± 0.1	3.1	1.5×10^{6}	1.5×10^{6} [a]
$C\,^3\Pi_u, v = 1$	3.5 ± 0.1	3.5	3.0 ± 0.1	3.1	8.7×10^{5}	9.8×10^{5}
$C\,^3\Pi_u, v = 2$	3.5 ± 0.1	3.5	3.0 ± 0.1	3.0	3.0×10^{5}	3.1×10^{5}

[a] Fitted to obtain n_0, cf text.

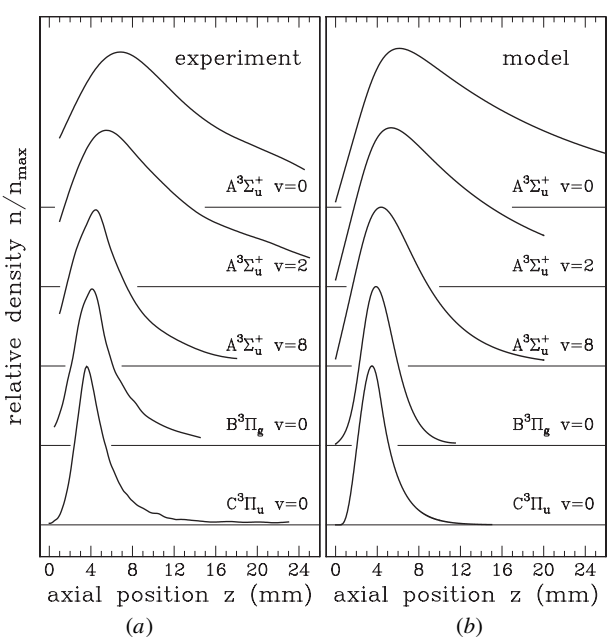

Figure 12. Standardized axial number density profiles $n(z)$ of the triplet states $A\,^3\Sigma_u^+$, $v = 0, 1, 2, 8$, $B\,^3\Pi_g$, $v = 0, 1, 2$ and $C\,^3\Pi_u$, $v = 0, 1, 2$: (*a*) experimental results and (*b*) results from the model; all at $p = 50$ Pa and $U_{eff} = 100$ V.

a slight discrepancy. Also the widths show a deviation only for these two long-lived states.

The maximum value of the absolute concentration n_{max} of the $C\,^3\Pi_u$, $v = 0$ state has been adjusted to the measured density by fitting the model parameter n_0, with the result that all three investigated vibrational levels of $C\,^3\Pi_u$ agree in this parameter fairly well. The results of n_{max} for $A\,^3\Sigma_u^+$, $v = 8$ differ by a factor of two. This can be explained by the underestimation of quenching by discarding reaction (16) due to the lack of knowledge about the vibrational distribution of the molecular ground state $X\,^1\Sigma_g^+$.

The differences for the long-lived state $A\,^3\Sigma_u^+$, $v = 0, 2$ are much larger (table 4). The calculated number densities are up to a factor of six lower than the experimental data. This must be explained by the fact that we have not taken all formation processes into account. In the frame of the first part of the model we only investigate the direct excitation from the vibrational ground state of $X\,^1\Sigma_g^+$. The excitation cross section for the $A\,^3\Sigma_u^+$, $v = 0$ state is then very low, due to the small Franck–Condon factor. But the Franck–Condon factor increases with the increasing vibrational level of $X\,^1\Sigma_g^+$. So the excitation rates from $X\,^1\Sigma_g^+$, $v \geqslant 1$ to $A\,^3\Sigma_u^+$, $v = 0$ may be larger than that from $X\,^1\Sigma_g^+$, $v = 0$ and we have an underestimation of the direct excitation rate of the lower vibrational level of the $A\,^3\Sigma_u^+$ state in our model. For the excitation rate of the $C\,^3\Pi_u$ state this effect is negligible, due to its Franck–Condon factor and the low density of the vibrationally excited $X\,^1\Sigma_g^+$.

Another formation process which is not included by the model is the impact of electrons in the plasma bulk. Due to the low electron temperature ($T_e \approx 1$ eV) in the bulk this only affects the formation of molecular states with low excitation energy levels such as the lower vibrational states of $A\,^3\Sigma_u^+$. The excitation of the much higher $C\,^3\Pi_u$ state by the plasma

electrons is negligible. This is corroborated by a comparison of the axial number density profiles of the $C\,^3\Pi_u$ state with that of the plasma density (figures 5 and 6).

The number density of the $B\,^3\Pi_g$ state is undercalculated by the model by a factor of two. This is caused by the density of $A\,^3\Sigma_u^+$ being too low and therefore the calculated formation of $B\,^3\Pi_g$ by reaction (12) being too low. If we insert the measured $A\,^3\Sigma_u^+$, $v = 0$ density instead of the calculated density into the formation process of $B\,^3\Pi_g$ by this reaction, the model results in the measured density of the $B\,^3\Pi_g$ state.

Altogether, the results can be interpreted as a confirmation of the assumptions made in the context of the model regarding the axial distribution, at least for $C\,^3\Pi_u$,$B\,^3\Pi_g$ and $A\,^3\Sigma_u^+$,$v = 8$. Although direct excitation of all triplet states nearly exclusively occurs by the pulsating electron front in the plasma sheath, the different species show greatly different axial number density profiles. The $C\,^3\Pi_u$ state is found in the sheath region due to its efficient excitation by sheath electrons and its short radiative lifetime. Because of their longer radiative and collisional lifetimes, the long-lived species can diffuse away from the sheath region. Their axial density profile therefore is influenced by the wall loss process due to collisions with the electrode. Their maximum density is shifted into the plasma bulk. This also applies to the $B\,^3\Pi_g$ and $A\,^3\Sigma_u^+$, $v = 8$ states, albeit less so, due to their radiative and collisional lifetimes respectively being of the order of only microseconds.

5. Summary and outlook

The axial number density profiles of the three nitrogen molecule triplet states $A\,^3\Sigma_u^+$, $B\,^3\Pi_g$ and $C\,^3\Pi_u$ in various vibrational levels were measured by LIF and OES experiments in an asymmetric rf discharge. In combination with a Rayleigh scattering experiment in the same apparatus, the LIF intensities could be calibrated on an absolute scale which was the topic of another previous publication [10].

The species have shown unexpectedly different spatial distributions. These varieties can be explained using a simple model which takes into account diffusion, quenching and cascade processes as well as the excitation in the rf plasma sheath. The model indicates that $B\,^3\Pi_g$ and $C\,^3\Pi_u$ are formed exclusively in and by the pulsating sheath. In contrast the maximum density of the long-lived species $A\,^3\Sigma_u^+$, $v = 0$ is shifted into the plasma bulk because collisional deactivation at the surface of the electrode plays a more significant role due to diffusion.

Another interesting opportunity to verify the assumptions could be provided by time-resolved measurements of $C\,^3\Pi_u$ on a nanosecond timescale. This could demonstrate the temporally varied excitation by the pulsating sheath edge.

Acknowledgments

We acknowledge the generous support by the Deutsche Forschungsgemeinschaft through the Innovationskolleg INK-2 'Methods and Material Systems for the Nanometer-Regime' at the Institute of Physics of the Chemnitz University of Technology where the experiments were performed. We are also grateful for the support to continue the investigations at the University Greifswald through the DFG-Sonderforschungsbereich 198.

References

[1] Wild C and Koidl P 1991 *J. Appl. Phys.* **69** 2909
[2] Borysow J and Phelps A V 1994 *Phys. Rev.* E **50** 1399
[3] Augustyniak E and Borysow J 1994 *J. Phys. D: Appl. Phys.* **27** 652
[4] De Benedictis S, Dilecce G and Simek M 1994 *J. Phys. B: At. Mol. Phys.* **27** 615
[5] Coitout H, Cernogora G and Magne L 1995 *J. Phys. III* **5** 203
[6] Pancheshnyi S V, Starikovskaia S M and Starikovskii A Y 1999 *J. Phys. D: Appl. Phys.* **32** 2219
[7] De Benedictis S, Dilecce G and Simek M 1998 *J. Phys. D: Appl. Phys.* **31** 1197
[8] De Benedictis S, Dilecce G and Simek M 1999 *J. Chem. Phys.* **110** 2947
[9] Bogen P 1983 *Proc. XVI Int. Conf. on Phenomena in Ionized Gases (Düsseldorf)* (invited papers) p 164
[10] Krames B, Glenewinkel-Meyer T and Meichsner J 2001 *J. Appl. Phys.* **89** 3115
[11] Meichsner J, Zeuner M, Krames B, Nitschke M, Rochotzki R and Barucki K 1998 *Surf. Coat. Technol.* **98** 1565
[12] Meichsner J, Zeuner M, Krames B, Nitschke M and Rochotzki R 1997 *Polymer Preprints, Am. Chem. Soc.* **38** 1095
[13] Krames B 2000 *PhD Thesis* TU Chemnitz, Germany
[14] Fons J T, Schappe R S and Lin C C 1996 *Phys. Rev.* A **53** 2239
[15] Borst W L and Chang S L 1973 *J. Chem. Phys.* **59** 5830
[16] Albritton D L, Schmeltekopf A L and Zare R N 1973 *Diatomic Intensity Factors* (New York: Harper and Row)
[17] Poparić G, Vićić M and Belić D S 1999 *Chem. Phys.* **240** 283
[18] Woodcock B, Busby J, Freegarde T and Hancock G 1985 *Proc. 7th. Int. Symp. Plasma Chemistry (Fukuoka Japan)* p 381
[19] Freegarde T G M and Hancock G 1997 *J. Phys. IV France* **7** C4 15
[20] Woodcock B K, Busby J R, Freegarde T G M and Hancock G 1997 *J. Appl. Phys.* **81** 5945
[21] Geigl M 1999 Private communication
[22] Adams S F and Miller T A 2000 *Plasma Sources Sci. Technol.* **9** 248
[23] Guerra V and Loureiro J 1997 *Plasma Sources Sci. Technol.* **6** 361
[24] De Benedictis S, Dilecce G and Simek M 1993 *Chem. Phys.* **178** 547
[25] Fujimoto T, Okuda S and Shimizu N 1988 *Mem. Fac. Eng. Kyoto Univ.* **50** 82
[26] Stewart I M 1994 *J. Phys. D: Appl. Phys.* **27** 1487
[27] Beier M 1997 Private communication
[28] De Benedictis S and Dilecce G 1995 *Chem. Phys.* **192** 149
[29] De Benedictis S and Dilecce G 1995 *Plasma Sources Sci. Technol.* **4** 212
[30] Piper L G 1988 *J. Chem. Phys.* **88** 6911
[31] Cernogora G, Hochard L, Touzeau M and Ferreira C M 1981 *J. Phys. B: At. Mol. Phys.* **14** 2977
[32] Polak L S, Slovetskii D I and Sokolov A S 1972 *Opt. Spectrosc.* **32** 247
[33] Hays G N and Oskam H J 1973 *J. Chem. Phys.* **59** 6088
[34] Piper L G 1988 *J. Chem. Phys.* **88** 231
[35] Cernogora G, Ferreira C M, Hochard L, Touzeau M and Loureiro J 1984 *J. Phys. B: At. Mol. Phys.* **17** 4429
[36] Young R A and John G A S 1968 *J. Chem. Phys.* **48** 895
[37] Levron D and Phelps A V 1978 *J. Chem. Phys.* **69** 2260
[38] Dreyer J W and Perner D 1973 *J. Chem. Phys.* **58** 1195
[39] Rotem A, Nadler I and Rosenwaks S 1981 *Chem. Phys. Lett.* **83** 281
[40] Plain A, Gorse C, Cacciatore M, Capitelli M, Massabieaux B and Ricard A 1985 *J. Phys. B: At. Mol. Phys.* **18** 843
[41] Anton H 1966 *Ann. Phys.* **18** 178
[42] Becker K H, Engels H and Tatarczyk T 1977 *Chem. Phys. Lett.* **51** 111
[43] Urosević V V, Bozin J V and Petrović Z L 1983 *Z. Phys.* A **309** 293
[44] Pancheshnyi S V, Starikovskaia S M and Starikovskii A Y 1998 *Chem. Phys. Lett.* **294** 523